Towards the Determination of Joint Volatility-Hygroscopicity Distributions: Development and Response Characterization for Single-Component Aerosol

Kate M. Cerully[1], James R. Hite, Jr.[2], Molly McLaughlin[1,*], and Athanasios Nenes [1,2]

(1) {School of Chemical and Biomolecular Engineering, Georgia Institute of Technology, Atlanta, GA}

(2) {School of Earth and Atmospheric Sciences, Georgia Institute of Technology, Atlanta, GA}

(*) {Currently at the Department of Civil and Environmental Engineering, Colorado State University, Fort Collins, CO}

Abstract

This work presents the development and characterization of a thermodenuder for the study and interpretation of aerosol volatility. Thermodenuder measurements are further combined with a Continuous-Flow Streamwise Thermal Gradient CCN Counter (CFSTGC) to obtain the corresponding aerosol hygroscopicity. The thermodenuder response function is characterized with monodisperse aerosol of variable volatility and hygroscopicity. The measurements are then interpreted with a comprehensive instrument model embedded within an optimization framework to retrieve aerosol properties with constrained uncertainty. Special attention is given to the interpretation of the size distribution of the thermodenuded aerosol, to deconvolute the effects of impurities and multiple charging, and to simplifications on the treatment of thermodenuder geometry, temperature, the cooling section, and the effects of curvature and uptake coefficient on inferred particle volatility. Retrieved vapor pressures are consistent with published literature and shown to be most sensitive to uncertainty in the accommodation coefficient.

1. INTRODUCTION

Organic aerosol (OA) constitutes a large fraction of the atmospheric aerosol burden, with global production estimates ranging from 50 to 100 Tg yr^{-1} (e.g., Pye and Seinfeld, 2010; Hallquist et al., 2009; Jimenez et al., 2009; Kanakidou et al., 2005). Secondary organic aerosol (SOA) is the result of gas-to-particle conversion of oxidized gas-phase precursors and constitutes a large fraction of OA. Understanding the gas-particle partitioning of atmospheric aerosol is necessary for effective OA modeling and prediction of the aerosol

budget (e.g., Donahue et al., 2009). Furthermore, understanding the contribution of SOA to aerosol number and hygroscopicity is important for prediction of cloud condensation nuclei (CCN) (e.g., Gantt et al., 2012; Riipinen et al., 2011; Lambe et al., 2011; Engelhart et al., 2011; Chang et al., 2010; Massoli et al., 2010; Asa-Awuku et al., 2009; Roelofs, 2008; Kanakidou et al., 2005).

The volatility of SOA has been a subject of intense study for years in both chamber and environmental field studies. For example, Cappa and Jimenez (2010) found that a large portion of the ambient OA mass in Mexico City was non-volatile, while Lee et al. (2010) discovered that most OA in a remote region near Finokalia in Crete, Greece, was semi-volatile. In chamber studies, Salo et al. (2011) found that aerosol ageing took place in the gas phase due to OH oxidation of semi-volatile organic compounds (SVOCs) and intermediate-volatility organic compounds (IVOCs) rather than by bulk or surface reactions. Furthermore, the effects of particle volatility on CCN number and activity have also been investigated. Riipinen et al. (2011) showed that neglecting ultrafine aerosol growth by organic condensation can result in large underpredictions of CCN concentrations. Asa-Awuku et al. (2009) showed that volatilization of organic aerosol in CCN chambers can bias observed CCN activity, hence raising the need for considering volatility effects in these measurements. These studies all involved the use of a thermodenuder, a heated laminar flow reactor that volatilizes particles and is typically followed by a cooling section containing adsorbing materials that prohibit re-condensation of volatilized vapors onto the aerosol. These measurements help constrain the volatility distributions of organic aerosol (Donahue et al., 2006) for a quantitative description of semi-volatile aerosol partitioning.

Several thermodenuder designs have been presented and analyzed in the literature (Faulhaber et al., 2009; Huffman et al., 2008; Fierz et al., 2007; An et al. 2007; Wehner et al., 2002; Burtscher et al. 2001). Design parameters involve the residence time in the heating section (e.g., Saleh et al., 2011; Fierz et al., 2007; An et al., 2007), the temperature profile in the heating section (e.g., Faulhaber et al., 2009; Huffman et al., 2008), the effectiveness of the cooling section (e.g., Fuentes and McFiggans, 2012; Saleh et al., 2011; Fierz et al., 2007), and the modeling approach used to interpret the data (e.g., Saleh et al., 2011; Cappa et al., 2010; Riipenen et al., 2010; Saleh and Shihadeh, 2007). Generally, the thermodenuder geometry and instrument flow rate are selected to give a desired residence time in the heating section of the thermodenuder. Attention has also been given to characterizing temperature profiles that develop in the heating section through, for example, the use of sand as insulating material (Wehner et al., 2002) and multiple heating zones (e.g., Faulhaber et al., 2011; Huffman et al., 2008). Studies by Saleh et al. (2011) and Fuentes and McFiggans (2012) have investigated the level of importance of the cooling section and the influence of mass loading on the re-condensation fraction of volatilized material.

Models have been developed to interpret thermodenuder data and usually invoke assumptions and approximations regarding the temperature and flow profiles in the heating section. Together with the aerosol concentration flowing through the instrument and the degree to which gas-particle equilibrium is satisfied in the thermodenuder

influences how approximations affect the inferred volatility distributions. Cappa et al. (2010) and Lee et al. (2010) approximate the thermodenuder temperature with a piecewise profile with constant radial temperature based on the experimental temperature profile of Huffman et al. (2008). Riipinen et al. (2010) assume a constant temperature throughout the thermodenuder. Both studies assume a developed parabolic velocity profile for laminar flow from the entrance of the thermodenuder. Fuentes and McFiggans (2012) use a plug flow approximation, though Cappa et al. (2010) shows that this leads to an overestimation of vapor pressure and underestimation of the enthalpy of vaporization as compared to assuming a parabolic radial velocity. The above suggests that simplifications in temperature, concentration and flow profiles may under certain conditions introduce important uncertainties in inferred vapor pressure. A need therefore remains for an operational model that fully resolves pressure, temperature, concentration and velocity flow fields within the thermodenuder, and, is coupled with a comprehensive treatment of volatilization kinetics with minimal simplifications.

Here we present a newly-developed thermodenuder system with a fully coupled simulation model framework. The thermodenuder is carefully designed to provide as stable and constant temperature profiles as possible. Size-resolved aerosol are used to characterize instrument response function (i.e., the change in aerosol size at several thermodenuder temperature set points). The instrument model is formulated to consider the temperature, volatilized vapor, flow variations and the size distribution of the volatilized aerosol at every point in the instrument. The model is then embedded within an optimization framework to determine optimal estimates of vapor pressures and enthalpy of phase change from volatility data. Thermodenuder measurements are combined with a Continuous-Flow Streamwise Thermal Gradient CCN Counter (CFSTGC) to provide a composition proxy for interpreting the instrument response function and help deconvolute the influence of particle impurities on instrument response.

2. INSTRUMENTATION

2.1 Thermodenuder design

A thermodenuder was constructed based on the original design of Wehner et al. (2002) and modifications of Huffman et al. (2008) (Figure 1). The instrument consists of a heating section, which allows semi-volatile components in the aerosol to volatilize, followed by a cooling section where the volatilized gas components are adsorbed onto activated carbon before exiting the instrument. The heating section consists of a stainless steel tube wrapped with 3 sections of heating tape (HTS/Amptek). The section is further wrapped with 1 inch high-temperature fiberglass insulation to prevent heat loss from the tube. Flow continues through the cooling section, a wire mesh tube surrounded by activated carbon (Calgon Carbon Corporation, AP4-60) and enclosed by a large stainless steel pipe, allowing volatilized components to pass through the mesh and adsorb onto the carbon. At either end of the casing are two stainless steel discs which are held together by threaded screws and sealed using a silicon O-ring (3.25 inch ID, 3.75 inch OD). The heating and cooling section are connected by a short section of Swagelok unions. Thermodenuder geometry allows for centerline residence times in the heating section of 35.7, 17.9, and 10.7 s for flow rates of 0.3, 0.6, and 1 L min^{-1}, respectively.

Temperature within the heating section is measured at the outer surface of the stainless steel tube using three thermistors (Panasonic, type NTC). The first thermistor is placed at the end of the first heating tape section; the other two thermistors are placed at the center of the second and third heating tape sections, respectively. Centerline temperatures were measured by disconnecting the cooling section and inserting a thin steel rod with a point thermocouple protruding 1 inch from the end of the rod at different points throughout the centerline of the heating tube. This method was also used to measure the inner wall temperature across the tube and is used as a boundary condition for the instrument model. A fourth thermistor is placed before the entrance of the thermodenuder to record the entering flow temperature. All thermistors are tightly fastened onto the tube using polyimide Kapton® tape (maximum temperature rating of 200°C).

Feedback control is used to maintain the temperature profile in the heating section. The three thermistors along the heating tube wall are connected to a data acquisition device (LabJack, model U12) in conjunction with an electronic A/D converter and a LabVIEW program developed for this purpose. This system controls each heating tape section by comparing thermistor outputs to a desired set point temperature (usually within 0.5°C) and continuously records all desired parameters throughout the entirety of the experiment. The duration and frequency of current sent to the electrical heating tape can be varied to change the speed of heating and minimize set point overshoot. To prevent a fire hazard from uncontrolled overheating (e.g., due to a LabVIEW or computer failure), thermal fuses rated for 125°C were installed in line with each heating tape power supply.

2.2 Thermodenuder characterization

Set point temperatures and resulting centerline temperatures in the heating section confirms reliable and well-controlled behavior (Figure 2a). The measured profiles reach the set points with less overshoot than in existing thermodenuder designs (e.g., Wehner et al., 2002; Huffman et al., 2008; Faulhaber et al., 2009). This overshoot was mainly avoided by moving the thermistor to the end rather than the center of the first heating tape section as the impact of entrance effects is accompanied by a lower wall temperature than in the developed region.

Particle transmission efficiency, a measure of the particles that are lost in the instrument mainly from Brownian diffusion and thermophoresis in the cooling section (Orsini et al., 1998; Wehner et al., 2002; Huffman et al., 2008), was measured using ammonium sulfate aerosol, which is nonvolatile at up to as low as 75°C (Clarke, 1991; Burtscher et al., 2001; An et al., 2007). As diffusional and thermophoretic effects are dependent on particle size, aerosol were size-selected using a differential mobility analyzer (DMA; Model 3081, TSI) then split to a concentration particle counter (CPC; Model 3010, TSI) and the thermodenuder. An additional CPC (Model 3010, TSI) located downstream of the thermodenuder measured the exiting particle concentration. Figure 2b shows particle transmission efficiency for particles ranging from 50 to 100 nm incurred at 30°C and 80°C in the thermodenuder. Measurements conducted at a flow rate of 1 L min^{-1} range between the predicted diffusional losses (at 30°C) determined for a cylindrical tube (Hinds, 2009) at 1 L min^{-1} and results from both Huffman et al. (2008) and Wehner et al. (2002) measured at 0.6 L min^{-1}. This meets expectations and ensures that there are no

unanticipated particle losses from secondary flows or non-uniform temperature distributions in the instrument.

3. METHODOLOGY

3.1 Experimental setup

CCN activity and hygroscopicity of denuded and non-denuded aerosol are obtained using a DMT CFSTGC (Figure 3) (Lance et al., 2006). Particles with a critical supersaturation less than the water vapor supersaturation, *s*, in the CFSTGC will activate into cloud droplets and be counted as CCN. We use the Scanning Flow CCN Analysis (SFCA) method of operation (Moore and Nenes, 2009) that allows high-resolution measurements of CCN concentration as a function of *s* over short periods of time. CCN measurements in this study are used to provide a proxy for chemical composition; although particles generated here are theoretically composed of one compound, impurities in the chemicals and water used during the particle generation process may affect particle volatility (especially when considerable volatilization is seen) and should be reflected in the CCN activity (Sections 4.1 and 4.3).

In the instrument setup used, compounds in solution with deionized water are atomized. The droplet stream passes through two silica gel diffusion dryers, and the resulting dried particles are charge-neutralized by a Kr-85 (Model 3077A, TSI) or Po-210 bipolar charger source before entering a DMA. Filtered dilution air is introduced to the size-resolved aerosol stream before splitting to a CPC and computer-controlled three way valve that allows the stream to flow through the thermodenuder or a bypass line. This configuration enables us to operate as a combined Volatility Tandem DMA (Orsini et al., 1998; Rader and McMurry, 1986) and size-resolved CCN activity spectrometer. Additional dilution air is introduced before the flow is split to a scanning mobility particle sizer (SMPS; consisting of a DMA and CPC) which measures the aerosol size distribution exiting the thermodenuder system, and to a laminar flow box and the CFSTGC, which gives the total number of activated particles (i.e., CCN). The laminar flow box is used to maintain a constant flow (1 L min^{-1}) which is introduced into the CFSTGC as needed, because the sample flow in CFSTGC column is constantly changing during SFCA operation. Accurate balancing of flows throughout the system is critical; the addition of an extra filter and valve open directly to room air after the thermodenuder and before the SMPS and SFCA systems ensures that there is no over- or under-pressurization of the flow lines during operation. All DMAs are operated with a sheath flow rate of 10 L min^{-1} and aerosol flow rate of 1 L min^{-1}. The top-to-bottom temperature difference in the CCN instrument is maintained at 12°C. Flow in the SFCA was linearly ramped from 0.2 to 0.9 L min^{-1} then back down to 0.2 L min^{-1} over 60 seconds, resulting in a CCN spectrum between ~0.30 to 0.80% *s*.

3.1.1 Thermodenuder measurements

Polydisperse particles composed of pure organic acids that span almost 7 orders of magnitude in vapor pressure (Table 2), including straight chain dicarboxylic acids (adipic acid, Fisher Scientific, 99% purity; azelaic acid, City Chemical LLC, 98% purity; malonic acid, Fisher Scientific, reagent grade; pimelic acid, Acros Organics, 99% purity; suberic acid, Acros Organic, 99% purity; succinic acid, Acros Organics, 99% purity) are

first classified by a DMA. Particle concentration is then measured by a CPC before entering the thermodenuder (Figure 3). A SMPS measures the size distribution at the exit of the thermodenuder and concentration is given by the integrated concentration of the entire measured size distribution. Analysis of the entire distribution of the denuded aerosol is used to characterize the instrument response function (Section 3.2), from which a characteristic mode diameter given by the SMPS size distribution is used to represent the exiting aerosol size for volatility and hygroscopicity interpretation.

The aerosol sampling schedule is outlined in Figure S1. Aerosol flow is automatically switched between the non-denuded bypass line (By) and thermodenuder line (TD) every 9 minutes. Aerosol sizes of approximately 70 to 150 nm are selected and allowed to flow through the system for 18 minutes each (9 minutes each from the bypass and thermodenuder). Three SMPS scans lasting for 135 s each (120 s for each upward voltage scan and 15 s for the downscan) are run consecutively 3 times for the bypass line and thermodenuder, respectively. The first SMPS scan begins 2 minutes into each 9 minute cycle, allowing time for the desired classified aerosol sample to flush through the instrumentation. Temperature in the thermodenuder is held constant until all sizes have been measured from both the bypass and thermodenuder; the temperature set point is then changed and requires 4 to 5 minutes to re-equilibrate (within 0.5°C) before the aerosol measurement cycle is repeated.

3.1.2 Obtaining size-resolved hygroscopicity

The ratio of CCN to CN concentration, termed the activation ratio, is expressed against instantaneous flow rate at each second during a SFCA upscan (downscans were not used in this study), to yield a curve that is fit to a sigmoidal activation ratio function (Moore and Nenes, 2009). The resulting critical flow rate, Q^*, where half of the CN are activated, is then determined. Flow rate, Q, is related to a characteristic supersaturation, s^*, using the calibration method described in Moore and Nenes (2009). s^* is then used to characterize the denuded aerosol hygroscopicity parameter, κ (Petters and Kreidenweis, 2007)

$$\kappa = \frac{4A^3}{27 d_p^3 s^{*2}} \quad (1)$$

where $A=(4M_w\sigma_w)/(RT\rho_w)$, and M_w, σ_w, and ρ_w are the molar mass, surface tension, and density, respectively, of water at the average mid-column temperature, T, in the CFSTGC (~306 K). R is the universal gas constant, and d_p is the characteristic diameter of the denuded aerosol.

3.2 Modeling of thermodenuder and aerosol response

The thermodenuder model consists of one module that determines the flow, temperature and volatilized organic vapor distribution inside the heating section for a given temperature and flow rate set point and another that simulates the semi-volatile partitioning of aerosol during its residence in the instrument. The modules can be separately executed, providing the advantage of resolving the flow and temperature fields once for a given set point for multiple inputs into the aerosol module.

The instrument model considers the full geometry of the flow, including the heating section, fittings, and cooling section. The axisymmetric gridding system, example fluid streamlines and aerosol sizes along them are presented in Figure 4. The influence of

particle loading and proximity to the heating section walls is evident. Particles closest to the walls experience the most volatilization, owing to their relatively longer residence time in the heating section (see Supplementary Material, Figure S7). As expected, higher particle mass loadings lead to accumulation of volatilized vapors in the thermodenuder, which depresses the driving force for aerosol volatilization.

3.2.1 The flow field module

The flow and temperature fields in the instrument are determined by numerically solving the Navier-Stokes, energy and volatilized species conservation equations at steady state (Supplementary Material A). The equations are solved using a finite-volume formulation that uses a hybrid upwind-central differencing scheme to compute the convective/diffusive fluxes over each finite volume. The velocity grids are staggered with respect to the scalar field grids to ensure consistency in the pressure fields obtained during the solution. Solution of the hydrodynamic cycle (velocity and pressure fields) is obtained using the Semi-Implicit Method for Pressure Linked Equations (Patankar, 1980). A uniform grid was used for each variable, with 100 grid cells for each spatial coordinate, which ensures a solution that agrees to within a few percent of the asymptotic (with respect to grid density) limit (Figure 4). The boundary conditions to the flow problem are the inlet flow rate and the wall temperature profile obtained from the normalized, measured thermodenuder axial centerline temperature profiles, scaled to the set point temperature (Figure 2a). Fully solving the velocity and pressure fields requires considerable computational time which is acceptable as the resulting flow field is calculated once and then stored for repeated use by the aerosol module. Examples of velocity, concentration and saturation fields are presented in Figure 4.

3.2.2 The aerosol module

The aerosol module treats the dynamic semi-volatile partitioning between the vapor and condensed (aerosol) phase. Aerosol volatilization is considered by Lagrangian tracking of particles along each streamline in the thermodenuder flow field; local conditions of temperature and gas-phase concentration of organic compounds are then used in the solution of the particle-to-gas mass transfer equations presented below. The aerosol distribution for each streamline is discretized into a number of aerosol size bins, each with a characteristic diameter and number concentration; each bin is then separately treated in terms of mass transfer through the gas phase. Coupling of the locally volatilized/condensed mass from/to the aerosol is accomplished through an iterative procedure with the gas-phase equations (see Supplementary Material A). The chemical composition for each aerosol section may be treated independently; one set of values is used in this study for all sections, leaving the treatment for chemically complex aerosol for a future study.

Gas-to-particle mass transfer is described with the following equation (Seinfeld and Pandis, 2006):

$$d_p \frac{d(d_p)}{dt} = \frac{\frac{P_\infty}{P^o} - \exp\left(\frac{4M\sigma}{R\rho D_p T_\infty}\right)}{\frac{\rho R T_\infty}{4\mathcal{D}_{AB} M P^o \Phi} + \frac{\Delta H \rho}{4kT_\infty}\left(\frac{\Delta H M}{RT_\infty} - 1\right)} \quad (2)$$

where T_∞ is the local air temperature inside the thermodenuder, P^o is the saturation vapor pressure of the volatilizing species at T_∞, P_∞ is the local vapor pressure of the volatilizing

species, ΔH is its specific enthalpy of phase change of the volatilizing vapor, and R is the ideal gas constant. ΔH could represent either the enthalpy of vaporization or sublimation, depending on the phase of the volatilizing aerosol. ρ, d_p, M, and σ are the density, diameter, molar mass, and interfacial energy of the aerosol, respectively. The thermal conductivity of air is represented by k. D_{AB} is the diffusivity of the volatilizing species (B) in air (A). Φ is the value of the Fuchs-Sutugin correction factor for non-continuum effects (presented below).

The saturation vapor pressure for the aerosol is assumed to follow the Clausius-Clapeyron relationship:

$$P^o(T_\infty) = P^o(T_o)\exp\left[\frac{\mathrm{M}\Delta H}{R}\left(\frac{1}{T_o}-\frac{1}{T_\infty}\right)\right] \quad (3)$$

where T_o = 298K. ΔH is assumed to be constant over the temperature range considered and is treated as a fitting parameter for the model optimization. Including the temperature dependence of ΔH would potentially introduce a large uncertainty in the retrieved heat capacity unless a wide range of temperature is considered, so it is not considered here.

The thermal conductivity, k, of air corrected for non-continuum effects is given by

$$k = \frac{k_a}{1+\frac{2k_a}{\alpha_T d_p \rho c_p}\left(\frac{2\pi M_a}{RT_\infty}\right)^{1/2}} \quad (4)$$

where k_a is the thermal conductivity of air in the continuum regime, $k_a = 10^{-3}(4.39 + 0.071T_\infty)$ with units of J m^{-1} s^{-1} K^{-1}, c_p is the specific heat capacity of air (1006.1 J kg^{-1} K^{-1}), and α_T is the thermal accommodation coefficient, here considered to be unity (Seinfeld and Pandis, 2006). M_a is the molar mass of air (0.029 kg mol^{-1}).

Existing studies that employ a kinetic model for evaporation in a thermodenuder make various assumptions regarding the diffusion coefficient, D_{AB}. For aerosol of known composition, the Hirschfelder, Bird, and Spotz formula (Bird, 2002) is often employed using available Lennard-Jones parameters (e.g., Bilde et al., 2003). A constant diffusion coefficient may be prescribed in the investigation of more complex mixtures or to generalize instrument conditions (e.g., Fuentes and McFiggans, 2012; Cappa and Jimenez, 2010). In this study, the method of Fuller et al. (1966) is used to compute D_{AB} (cm^2 s^{-1}) for a binary mixture of air (A) and the evaporating component (B):

$$D_{AB} = \frac{10^{-3}T^{1.75}\left(\frac{1}{M_A}+\frac{1}{M_B}\right)^{1/2}}{P\left(v_A^{1/3}+v_B^{1/3}\right)^2} \quad (5)$$

where v_A and v_B are the empirically-defined "diffusion volumes" for species A and B, respectively. For a particular molecule, Fuller et al. (1966) provide correlations for computing the diffusion volume as the sum of contributions from individual atoms along with modifications for certain structural features (e.g., rings). A study considering diffusivities of low volatility compounds in various background gases (Ravindran, 1979), found that it was a comparably accurate estimation technique for diffusion in low molecular weight carrier gases, being outperformed only by one other empirical fit to diffusional data. The calculated diffusion volumes for each compound in this study are provided in Table 1 along with corresponding densities and molecular weights.

The Fuchs-Sutugin non-continuum correction factor, Φ, in Equation (2) is given by (Seinfeld and Pandis, 2006; Fuchs and Sutugin, 1971):

$$\phi = \frac{0.75\alpha(1+\mathrm{Kn})}{\mathrm{Kn}^2+\mathrm{Kn}+0.283\mathrm{Kn}\alpha+0.75\alpha} \quad (6)$$

where $\mathrm{Kn} = \frac{2\lambda_{AB}}{D_p}$ is the Knudsen number, and the mean free path, λ_{AB}, of the volatilizing compound in air is $\lambda_{AB} = \frac{3D_{AB}}{\bar{c}_B}$, where $\bar{c}_B$ is the thermal speed of the gas phase component, $\bar{c}_B = \left(\frac{8RT}{\pi M_B}\right)^{1/2}$, and α is the uptake (evaporation) coefficient.

Equation (2) is numerically integrated using the DVODE (Variable-coefficient Ordinary Differential Equation solver) (Brown, 1989) to determine the diameter of aerosol particles when they exit the instrument. This is done for each streamline, initializing the particle size to the DMA-observed inlet condition. Particles are then allowed to follow each streamline, based on the local value of velocity (in both axial and radial directions). During the integration of Equation (2), thermophysical parameters are allowed to vary based on the temperature variations experienced by the particles as they flow through the instrument. The volume-weighted average exit diameter from the heating section is taken as the modeled outlet diameter, d_{pm},

$$d_{pm} = \bar{d}_{p,v} = \frac{\int_0^{R_{TD}} d_p u_z r\, dr}{\int_0^{R_{TD}} u_z r\, dr} \quad (7)$$

where u_z represents the axial velocity at the exit of the heating section, r is the radial distance from the centerline, R_{TD} is the inner radius of the heated section, and d_p is the particle diameter at the end of each streamline. These model output diameters, along with the observed final aerosol diameters, are utilized in the optimization routine to retrieve optimal estimates of volatility parameters. Examples of predicted aerosol size profiles with the fully-coupled model are provided in Figure 4. As aerosol loading increases, less of the particle volatilizes owing to the increasingly saturated state of the gas phase.

Aerosols were assumed to be spherical with physical diameter equal to their mobility diameter. Irregularly-shaped aerosol can be accounted for by the inclusion of a shape factor, χ. For instance, a previous study found χ for solid (crystalline) adipic and azelaic acid aerosol to range between 1.05 and 1.1 (Saleh et al., 2010). While this estimated shape factor is not representative of all OA, it provides a possible range of systematic correction to the DMA sizing required. Aerosol in this study is generated from atomization of an unsaturated solution at room temperature, and it is postulated that the dried aerosol are sufficiently amorphous considering the short drying time allowed, compared to experimental conditions in the study of Saleh et al. (2010). Salo et al. (2010) indicated that solvent inclusions are unlikely to be present in aerosol generated with a drying setup similar to Saleh et al. (2010), although the hysteresis of aerosol efflorescence and the formation of eutectics allows for the presence of both liquid and solid phase aerosol. Calculations of volatility parameters for separate measurements suggest that this occurred for pimelic acid in their experiments. With these results in mind, the aerosol generated in this study can likely be considered an amorphous solid, although the vapor pressure retrievals may be sensitive to the aerosol phase state.

3.2.3 Optimal estimation of volatility parameters and uncertainty

Optimal estimation of the parameters used in the evaporation model is accomplished through the use of the Levenberg-Marquardt algorithm as implemented in the International Mathematical and Statistical Library subroutine ZXSSQ (Ver. 6/1/1982). The output diameter from the model is first calculated for an initial guess of volatility parameters. An objective function expressing the deviation between predicted and observed diameter is then minimized to yield optimal values of volatility parameters, as determined below.

Laboratory data was collected for each single component aerosol consisting of the inlet diameters ($d_{p,in}$) and associated outlet mode diameters ($d_{p,out}$) from the SMPS after the thermodenuder at three different temperature settings, T_{set}, with consistent flow rate settings, Q_{set}. Not all values of $d_{p,out}$, however, could be used owing primarily to the effects of impurities and multiple charging. The determination of the appropriate $d_{p,out}$ to be used in the model fitting is discussed in Section 4.2. If M independent observations (i.e. unique combinations of $d_{p,in}$, T_{set}, and Q_{set} for a particular aerosol) are available, N independent parameters (represented by the aerosol property vector, $\vec{x}^N$) can be optimally fit to the data, provided that N < M (for parameter robustness). Volatility parameters and uncertainty ranges for each organic acid investigated were obtained through the use of the ZXSSQ optimization routine coupled with the instrument model. The optimization routine minimizes the returned residuals of the aerosol module where the cost function is defined as

$$Q = \sum_{i=1}^{\mathrm{M}} \left(d_{p,out,i} - d_{pm,i}\right)^2 \quad (8)$$

where i = 1, … , M are the data points available for fitting with $d_{p,out}$ representing the observed diameter and d_{pm} is the diameter computed by the aerosol module.

In this study, optimal values for $P^o(T_o)$ and ΔH are obtained for the single component aerosol (N = 2), while other variables (i.e. density, molecular weight, diffusivity, and the accommodation coefficient) are constrained from literature values or estimated. The initial guesses used in the iterative optimization procedure were obtained from a more typical approach to TDMA data inversion (e.g., Salo et al. 2010, Rader & McMurry 1986).While it is possible to increase N provided a large enough value of M, doing so decreases the confidence of the fit and increases sensitivity to the initial guess of the parameter used in the iterative scheme. Thus, the more observations fit to the least number of parameters provides the most robust parameter estimates. The optimization method additionally provides an estimate of parameter uncertainty (see Supplementary Material B). It should be noted that both $P^o(T_o)$ and ΔH are simultaneously fitted to the all experimental data at various $d_{p,in}$, and T_{set} and for particular, fixed, values of the accommodation coefficient and surface free energy in the optimization algorithm, so no assumptions regarding the fitted parameter values are made *a priori* (see Supplementary Materials B).

4. RESULTS

Particles composed of single organic compounds with known properties were generated and introduced into the thermodenuder and SFCA to characterize the instrument response functions, or volatilization profiles, of input versus final particle size at several different temperatures in the thermodenuder. The instrument model is then used to interpret the profiles and retrieve volatility parameters that are compared against published literature values.

4.1 Volatility measurements

An example of size distribution evolution for a given classified organic component at three different thermodenuder temperatures is shown in Figure 5. As temperature becomes greater, increased volatilization results in the size distribution exiting the thermodenuder shifting to smaller sizes. Inlet and exit sizes for each compound studied at all temperatures considered are presented in the Supplementary Material (Figure S2). As expected, the thermodenuded particle size mode is a monotonic function of initial size; outlet particle size decreases as temperature is increased. In cases where particles are highly volatilized, final particle size reaches a lower limit of approximately 10 to 30 nm where further volatilization ceases (shown in Supplementary Figure S2). This size limit is the result of impurities in the organic compounds and water used for atomization and is described in detail in Section 4.2.

4.2 Interpreting the presence of multiple modes in thermodenuded size distributions

Investigation of measured size distributions exiting the thermodenuder suggest that as particles are heated, up to three different modes may emerge. This is concerning, as one particular outlet diameter should result from any given inlet diameter and thermodenuder temperature; deviations from this behavior, if due to instrument artifacts (e.g., a result of non-ideal flow or nucleation of supersaturated organic vapors in the cooling section) can bias retrieved volatility parameters. Understanding these modes requires a full understanding of the thermodenuder instrument response.

The smallest size mode is only observed when aerosols are highly volatilized and does not appear at relatively lower temperatures (Figure 5). Non-volatile components in the particle would leave behind a detectable residual particle when the organic fraction has completely volatilized. This explains the presence of bimodal distributions (Figure 5), as the organic aerosol flowing along streamlines close to the thermodenuder wall volatilizes completely, leaving behind the non-volatile mode while those nearest the centerline are not heated for enough time, consistent with the vapor source rates shown in Figure 4. The lower size mode diameter does not appear to vary with temperature set point, indicating that it indeed reflects remnant low-volatility material, as otherwise the particles would further shrink or disappear as temperature is increased. Analysis of the size of the aerosol obtained through the reported compound impurity yields particles consistent with the measured size (Supplementary Material C, and Sato et al., 2010). Nucleation of supersaturated vapor at the exit of the heating section also is also an unlikely source of the small particles, as suggested by the analysis of the experimental data (Supplementary Material C). The largest mode present can consistently be attributed to the presence of doubly-charged particles. Indeed, the simulations yield output diameters consistent with

the largest mode for all species considered, even when the doubly-charged size is used as the initial condition (Supplementary Material C).

Based on the above discussion, the mode diameter used for volatility calculations was the middle mode when a tri-modal distribution was present. Additionally, unimodal data within the range of the non-volatile core were discarded; bimodal data with an observable mode larger than that of the non-volatile core utilized the large mode size.

4.3 Fitted volatility parameters, uncertainties, and literature comparison

Volatility parameters and associated uncertainties were obtained inform the model fitting procedure (Section 3.2.3). The optimal parameters for each compound that presented the least residuals against the laboratory data out of the various initial conditions were taken as the model fits and are presented in Table 2. For each compound considered, the observed inlet and outlet diameters are plotted alongside the fitted model response in Figure 6. Here, solid curves represent the model evaluated at one set of the optimized parameters from Table 2. The dashed curves are model evaluations made at the upper and lower bounds of the uncertainty ranges in the retrieved parameters. Open circles are the raw data – the maximum mode diameter – initially obtained from the SMPS size distributions. Starred points are the data that was actually used in the model fitting, adjusted according to discussion of Section 4.2. The inclusion of the unfitted data illustrates the consistency of the thermodenuder model, as the model outlet diameter is either lower than or equal to the observed non-volatile diameters within the uncertainty of the volatility parameter estimate.

In the model optimizations, the literature value used for the interfacial energy was varied to assess the sensitivity of the retrieved parameters. The uptake/evaporation coefficient was assumed to be unity by default but was also varied to literature values in Table 1 when available. Figure 7 presents the results of the uncertainty analysis and compares the fitted parameters with published data. Blue points with red numbers in each plot represent the results of the model runs indicated in Table 2 where the values for interfacial energy and (in two cases) uptake coefficient were varied. Additional simulations were carried out to assess the sensitivity of these results to the model geometry (inclusion of the cooling section), impact of varying the accommodation coefficient for all data, and oscillations in the wall temperature profile and inlet temperature on the order of experimental observations. For all compounds, changes in interfacial energy vary the retrieved values of P^o and ΔH to within uncertainty. This is consistent with a low impact of the Kelvin effect on equilibrium vapor pressure for sizes larger than those corresponding to non-volatile cores in the data. Put together, these results indicate that for our experimental conditions, only the sensitivity to choice of accommodation coefficient had a significant impact (outside of estimated error ranges) on the retrieved $P^o(T_o)$, corresponding to a direct proportionality between the two parameters (see the Supplementary Materials, Figure S7).

In general, retrieved parameters for adipic acid are within the literature spread of volatility parameters. The optimal parameters for azelaic acid appear to be in the appropriate range for P^o but with slightly lower ΔH than the available literature. Optimal

parameters for malonic acid (Figure 7c) agree to within uncertainty with Riipinen et al. (2007). Results for succinic acid (Figure 7f) appear consistent with estimates of solid P^o from various literature sources. Adjusting the accommodation/evaporation coefficient resulted in a significant change in the fitted parameters, placing it in agreement with the results of Saleh et al. (2009). The model fitting for pimelic acid is not possible, since only points at one temperature set point were uninfluenced by insoluble cores and available for fitting (Figure 6f). Thus, the numeric results for the fitted volatility parameters are not included in Table 2 or Figure 7. Suberic acid results are subject to large uncertainty (Table 2, Figure 7e) owing to the limited volatilization observed. This occurred because the observed size change of the aerosol was smaller than the uncertainty range obtained from the DMA transfer function for the inlet diameters for all but three of the data points. Thus the optimal parameter uncertainties calculated by propagating the measurement uncertainty through the Jacobian returned by the optimization routine (see Supplementary Material B) yielded very large values because the perturbation used ($\Delta d_{p,in}$) was greater than the observed size change used to fit the model. However, the estimate still provides an upper limit on suberic acid volatility which is in agreement with the Bilde et al. (2003) P^o and ΔH values.

An interesting aspect of the analysis is in the effect of particle phase on vapor pressure. Given the potentially large difference between vapor pressure between a solid and supercooled liquid substance (at the same temperature), comparison of the fitted model volatility parameters to the available literature data for solid and liquid phases of the components can potentially be used to follow the phase transitions through an experiment. The resulting phase change (vaporization if liquid, or sublimation if solid) could be concluded based on the literature comparison since either follow the Clausius-Clapeyron relationship, and, the use of the Kelvin effect as formulated in Equation (2) would be valid for either a liquid or amorphous solid aerosol (Tao and McMurray, 1989). For example, the succinic acid aerosol generated in this study behaved most consistently with being a solid. If vapor pressure inferences are accompanied with a more accurate and direct methods exist to determine particle phase (e.g., Virtanen et al., 2010), then one could confirm the above and also provide an important affirmation of the modeling framework and instrument data analysis.

4.5 Aerosol hygroscopicity

As only pure components are sampled and temperature does not vary considerably, κ should remain effectively constant through each experiment regardless of size and sampling from the bypass line or thermodenuder. κ values are calculated for each compound and averaged for all particle size and temperature measurements from the bypass, κ_{By}, thermodenuder, κ_{TD}, and bypass and thermodenuder combined, κ_{Tot} (Table 3). When a significant fraction of multiply charged particles are present in the CFSTGC, activation will begin at a lower critical supersaturation in the instrument, impacting the calculation of κ using Equation (1). This can be avoided by correcting the sigmoidal fitting curve for multiply charged particles (e.g., Moore et al., 2010; Moore and Nenes, 2009). Impurities in the chemical compounds or water used for atomization may potentially impact the κ of highly volatilized particles when the volume fraction of the impurity becomes large enough. The consistent values of κ, indicated by both the

averages and standard deviations in κ measured for a given compound in the bypass and thermodenuder, confirm the non-volatile residuals do not impact total κ measurements as they are not present in sufficient amounts, or, exhibit similar κ to the pure compound. In the case of the non-volatile residual particles, Equation (1) shows that at the highest supersaturations in the instrument (~0.80%), even a highly hygroscopic, pure salt particle such as NaCl ($\kappa \approx 1.2$; Petters and Kreidenweis, 2007) would need to have a diameter of at least 25 nm to activate. Though residual particle sizes larger than 25 nm could theoretically activate based on the previous calculations if they had a high value of κ, no thermodenuded particles less than approximately 70 nm in diameter are shown to activate into CCN, indicating that the non-volatile residuals exhibit low hygroscopicity.

All experimental values of κ agree to uncertainty with reported literature values. There is no clear shift to higher or lower κ values between the measured values and the range of literature values, further demonstrating that the potentially increased presence of impurities during the volatilization of particles does not appear to cause a particular shift in hygroscopic behavior of the measured compounds.

5. CONCLUSIONS

A thermodenuder with active temperature control has been constructed and characterized for steady temperature profiles and particle transmission efficiency. The system is characterized by the measured response of pure component organic aerosol with volatility spanning roughly 7 orders of magnitude in vapor pressure and is integrated with a comprehensive model that combines a computational fluid, mass, and heat transfer module integrated with a gas-phase module, with an optimization framework to infer thermo-kinetic parameters of the denuded aerosol to obtain CCN behavior and aerosol hygroscopicity information. For each volatile compound, particle size decreases as temperature increases. Measured aerosol hygroscopicity, as expected, is consistent for each pure compound at different sizes and temperatures.

The presence of three potential size modes exiting the thermodenuder due to non-volatile material in the aerosol, the dominant size-selected aerosol, and multiply charged particles, respectively, is carefully considered in the analysis. Non-volatile material in the aerosol sample impact volatilization profiles for highly volatilized particles, leaving a small residual particle of ~10 to 30 nm, though this can be explained by the level of impurities found in chemical compounds and water used to atomize the aerosol particles. These residuals are shown to have no impact on the measured hygroscopicity, though caution should be taken to investigate the impacts of impurities on measured properties in all relevant laboratory studies involving atomization of “pure” compounds. Size modes due to non-volatile material and multiply charged particles are deconvolved and not considered in the analysis.

In general, the volatility parameters retrieved in this study compare well with the literature. Adjusting the uptake coefficient to reported values for succinic and adipic acids results in the retrieval of volatility parameters that are in agreement with literature values. This suggests that the same response of aerosol within the thermodenuder can result in estimates of thermodynamic parameters that vary over orders of magnitude depending on the assumptions regarding the evaporation kinetics.

Future work will focus on determining volatility-hygroscopicity distributions using multi-component laboratory measurements and further augmenting the model with a full implementation of the volatility basis set approach. An adaptive measurement technique based on a simplified kinetic model from one of several approaches in the literature that can check the extent of the size change in real time and adjust selected sizes and temperature set points according to the anticipated volatility would further reduce biases in the retrieved volatility parameters. Avoiding the re-equilibration of the charge distribution at the second DMA would allow for a simpler analysis of the measured SMPS distributions (Rader and McMurry, 1986), since changes in the mobility distribution would be constrained to changes in their physical size alone. Finally, an important affirmation of the modeling framework and instrument data analysis would be to relate vapor pressure changes with a particle phase changes measured with another technique (e.g., Virtanen et al., 2010). This would require the kinetic parameter to be constrained independently and may be challenged by the effects of chemical impurities, but it is possible, provided ample control of experimental conditions and complimentary modeling of the physical system.

The use of low thermodenuder temperatures and small aerosol sizes are strong advantages as it ensures sensitivity to small amounts of volatilized aerosol and avoids excessive chemical transformation of the sample from heating. Together with the comprehensive model and its demonstrated performance, the work presented here is a powerful tool for volatility/hygroscopicity studies at atmospherically-relevant mass loadings.

Acknowledgments
The authors acknowledge support from NOAA and NASA. A Georgia Institute of Technology UROP Materials and Supplies Grant, a Georgia Institute of Technology President Undergraduate Research Award, and an Air Products Undergraduate Research Grants are also gratefully acknowledged.

References
An, W. J., Pathak, R. K., Lee, B. H. Pandis, S. N. (2007). Aerosol volatility measurement using an improved thermodenuder: Application to secondary organic aerosol. J. Aerosol Sci. 48:305-314.

Asa-Awuku, A., Engelhart, G. J., Lee, B. H., Pandis, S. N., Nenes, A. (2009). Relating CCN Activity, Volatility, and Droplet Growth Kinetics of β-caryophyllene Secondary Organic Aerosol. Atmos. Chem. Phys. 9:1–18.

Bilde, M., Svenningsson, B., Mønster, J., Rosenørn, T. (2003). Even-odd alternation of evaporation rates and vapor pressures of C3-C9 dicarboxylic acid aerosols. Environ. Sci. Tech. 37:1371.

Bird, R. B., Stewart, W. E., Lightfoot, E. N. (2002). Transport Phenomena (2nd ed.), New York, NY: John Wiley & Sons, Inc.

Booth, A. M., Markus, T., McFiggans, G., Percival, C. J., McGillen, M. R., Topping, D. O. (2009). Design and construction of a simple Knudsen Effusion Mass

Spectrometer (KEMS) system for vapour pressure measurements of low volatility organics, Atmos. Meas. Tech. 2:355-361.

Booth, A. M., Barley, M. H., Topping, D. O., McFiggans, G., Garforth, A., Percival, C. J. (2010). Solid state and sub-cooled liquid vapor pressures of substituted dicarboxylic acids using Knudsen Effusion Mass Spectrometry (KEMS) and Differential Scanning Calorimetry, Atmos. Chem. Phys. 10:4879-4892.

Booth, A. M., Montague, W. J., Barley, M. H., Topping, D. O., McFiggans, G., Garforth, A., and Percival, C. J. (2011). Solid state and sub-cooled liquid vapor pressures of cyclic aliphatic dicarboxylic acids, Atmos. Chem. Phys. 11:655-665.

Broekhuizen, K., Kumar, P. P., and Abbatt, J. P. D. (2004). Partially soluble organics as cloud condensation nuclei: Role of trace soluble and surface active species, Geophys. Res. Lett. 31:L01107. doi:10.1029/2003GL018203.

Brown, P. N., Byrne, G.D., and Hindmarsh, A. C. (1989). VODE, a variable-coefficient ODE solver, SIAM J. Sci. Comput. 10:1038–1051.

Burtscher, H., Baltensperger, U., Bukowiecki, N., Cohn, P., Hüglin, C., Mohr, M., Matter, U., Nyeki, S., Schmatloch, V., Streit, N., Weingartner, E. (2001). Separation of volatile and non-volatile aerosol fractions by thermodesorption: instrumental development and applications, J. Aerosol Sci. 32:427-442. doi:10.1016/S0021-8502(00)00089-6.

Cappa, C. D. (2010). A model of aerosol evaporation kinetics in a thermodenuder. Atmos. Meas. Tech. 3:579-592. doi:10.5194/amt-3-579-2010.

Cappa, C. D., Jimenez, J. L. (2010). Quantitative estimates of the volatility of ambient organic aerosol, Atmos. Chem. Phys. 10:5409-5424. doi:10.5194/acp-10-5409-2010.

Cappa, C. D., Lovejoy, E. R., Ravishankara, A. R. (2007). Determination of evaporation rates and vapor pressures of very low volatility compounds: A study of the C_4-C_{10} dicarboxylic acids. J. Phys. Chem. 111:3099-3109.

Cerully, K. M., Raatikainen, T., Lance, S., Tkacik, D., Tiitta, P., Petäjä, T., Ehn, M., Kulmala, M., Worsnop, D. R., Laaksonen, A., Smith, J. N., Nenes, A. (2011). Aerosol hygroscopicity and CCN activation kinetics in a boreal forest environment during the 2007 EUCAARI campaign. Atmos. Chem. Phys. 11:12369-12386, doi:10.5194/acp-11-12369-2011.

Chattopadhyay, S., Tobias, H. J., Ziemann, P. J. (2001). A method for measuring vapor pressures of low-volatility organic aerosol compounds using a thermal desorption particle beam mass spectrometer. Anal. Chem. 73:3797-3803.

Clarke, A. D. (1991). A thermo-optic technique for in-situ analysis of size-resolved aerosol physicochemistry, Atmos. Environ., 25:635-644.

Corrigan, C. E., Novakov, T. (1999). Cloud condensation nucleus activity of organic compounds: a laboratory study, Atmos. Environ., 33:2661-2668, doi:10.1016/S1352-2310(98)00310-0.

Cruz, C. N., Pandis, S. N. (1997). A study of the ability of pure secondary organic aerosol to act as cloud condensation nuclei, Atmos. Environ., 31:2205-2214, doi:10.1016/S1352-2310(97)00054-X.

Donahue, N. M., Robinson, A. L., Pandis, S. N. (2009). Atmospheric organic particulate matter: From smoke to secondary organic aerosol. Atmos. Environ. 43:94-106.

Donahue et al., N. M., Robinson, A. L., Stanier, C. O., Pandis, S. N. (2006). Coupled partitioning, dilution, and chemical aging of semivolatile organics. Environ. Sci. Tech. 40:2635-2643. doi:10.2012/es052297c.

Engelhart, G. J., Moore, R. H., Nenes, A., Pandis, S.N. (2011). CCN Activity of Isoprene Secondary Organic Aerosol, J. Geoph. Res. 116:D02207. doi:10.1029/2010JD014706.

Faulhaber, A. E., Thomas, B. M., Jimenez, J. L., Jayne, J. T., Worsnop, D. R., Ziemman, P. J. (2009). Characterization of a thermodenuder-particle beam mass spectrometer system for the study of organic aerosol volatility and composition. Atmos. Chem. Phys. 2:15-31.

Fierz, M., Vernooij, M. G. C., Burtscher, H. (2007). An improved low-flow thermodenuder. Aerosol Sci. 38:1163-1168.

Frosch, M., Bilde, M., DeCarlo, P. F., Jurányi, Z., Tritscher, T., Dommen, J., Donahue, N. M., Gysel, M., Weingartner, E., Baltensperger, U. (2011). Relating cloud condensation nuclei activity and oxidation level of α-pinene secondary organic aerosols. J. Geophys. Res. 116:D2212. doi:10.1029/2011JD01640.

Frosch, M., Zardini, A. A., Platt, S. M., Müller, L., Reinnig, M.-C., Hoffmann, T., and Bilde, M. (2010). Thermodynamic properties and cloud droplet activation of a series of oxo-acids, Atmos. Chem. Phys., 10:5873-5890, doi:10.5194/acp-10-5873-2010.

Fuentes, E., McFiggans, G. (2012). A modeling approach to evaluate the uncertainty in estimating evaporation behavior and volatility of organic aerosols. Atmos. Meas. Tech. 5:735-757. doi:10.5194/amt-5-735-2012.

Fuller, E. N., Schettle, P. D., Giddings, J. C., (1966). A new method for prediction of binary gas-phase diffusion coefficients. Ind. Eng. Chem. 58:18-57.

Gantt, N., Xu, J., Meskhidze, N., Zhang, Y., Nenes, A., Ghan, S. J., Liu, X., Easter, R., Zaveri, R. (2012). Global distribution and climate forcing of marine organic aerosol – Part 2: Effects on cloud properties and radiative forcing. Atmos. Chem. Phys. 12:6555-6563. doi:10.5184/acp-12-6555-2012.

Hallquist, M., Wenger, J. C., Baltensperger, U., Rudich, Y., Simpson, D., Claeys, M., Dommen, J., Donahue, N. M., George, C., Goldstein, A. H., Hamilton, J. F., Herrmann, H., Hoffmann, T., Iinuma, Y., Jang, M., Jenkin, M. E., Jimenez, J. L., Kiendler-Scharr, A., Maenhaut, W., McFiggans, G., Mentel, Th. F., Monod, A., Prévôt, A. S. H., Seinfeld, J. H., Surratt, J. D., Szmigielski, R., Wildt, J. (2009). The formation, properties and impact of secondary organic aerosol: current and emerging issues. Atmos. Chem. Phys. 9:5155-5236.

Hinds, William C. (1999). Aerosol technology: properties, behavior, and measurement of airborne particles (2nd ed.), New York, NY: John Wiley & Sons, Inc.

Hori, M., Ohta, S., Murao, N., Yamagata, S. (2003). Activation capability of water soluble organic substances as CCN. J. Aerosol. Sci. 34:419–448.

Huff Hartz, K. E. H., Tischuk, J. E., Chan, M. N., Chan, C. K., Donahue, N. M., Pandis, S. N. (2006). Cloud condensation nuclei activation of limited solubility organic aerosol. Atmos. Environ. 40:605–617.

Huffman, J. A., Ziemann, P. J., Jayne, J. T., Worsnop, D. R., Jimenez, J. L. (2008). Development and Characterization of a Fast-Stepping/Scanning Thermodenuder for Chemically-Resolved Aerosol Volatility Measurements. Aerosol Sci. Tech. 42:395-407.

Hyvärinen, A.-P., Lihavainen, H., Gaman, A., Vairila, L., Ojala, H., Kulmala, M., Viisanen, Y. (2006). Surface tensions and densities of oxalic, malonic, succinic, maleic, malic, and cis-pinonic acids. J. Chem. Eng. Data. 51:255.

International Mathematical and Statistical Library, Houston, Texas, (program IMSL-ZXSSQ).

Kanakidou, M., Seinfeld, J. H., Pandis, S. N., Barnes, I., Dentener, F. J., Facchini, M. C., Van Dingenen, R., Ervens, B., Nenes, A., Nielsen, C. J., Swietlicki, E., Putaud, J. P., Balkanski, Y., Fuzzi, S., Horth, J., Moortgat, G. K., Winterhalter, R., Myhre, C. E. L., Tsigaridis, K., Vignati, E., Stephanou, E. G., Wilson, J. (2005). Organic Aerosol and Global Climate Modelling: A Review. Atmos. Chem. Phys. 5:1053–1123.

Kumar, P. P., Broekhuizen, K., Abbatt, J. P. D. (2003). Organic acids as cloud condensation nuclei: Laboratory studies of highly soluble and insoluble species. Atmos. Chem. Phys. 3:509–520.

Kuwata, M., Shao, W., Lebouteiller, R., Martin, S.T. (2012). Classifying organic materials by oxygen-to-carbon elemental ratio to predict the activation regime of cloud condensation nuclei (CCN), Atmos. Chem. Phys. Discuss., 12:31829-31870, doi:10.5194/acpd-12-31829-2012.

Lambe, A. T., Onasch, T. B., Massoli, P., Croasdale, D. R., Wright, J. P., Ahern, A. T., Williams, L. R., Worsnop, D. R., Brune, W. H., Davidovits, P. (2011). Laboratory studies of the chemical composition and cloud condensation nuclei (CCN) activity of secondary organic aerosol (SOA) and oxidixed primary organic aerosol (OPOA). Atmos. Chem. Phys. 11:8913-8928. doi:10.5194/acp-11-8913-2011.

Lance, S., Medina, J., Smith, J. N., Nenes, A. (2006). Mapping the Operation of the DMT Continuous Flow CCN Counter. Aerosol Sci. Tech. 40:242-254.

Lee, B. H., Kostenidou, E., Hildebrandt, L. Riipinen, I., Engelhart, G. J., Mohr, C., DeCarlo, P. F., Mihalopoulos, N., Prevot, A. S. H., Baltensperger, U., Pandis, S. N. (2010). Measurement of the ambient organic aerosol volatility distribution: application during the Finokalia Aerosol Measurement Experiment (FAME-2008). Atmos. Chem. Phys. 10:12149-12160. doi:10.5194/acp-10-12149-2010.

Massoli, P., Lambe, A. T., Ahern, Williams, L. R., Ehn, M., Mikkilä, J., Canagaratna, M. R, Brune, W. H., Onasch, T. B., Jayne, J. T., Petäjä, T., Kulmala, M., Laaksonen, A., Kolb, C. E., Davidovits, P., Worsnop, D. R. (2010). Relationship between aerosol oxidation level and hygroscopic properties of laboratory generator secondary organic aerosol (SOA) particles. Geophys. Res. Lett. 37:L24801, doi:10.1029/2010GL045258.

Moore, R. H., Nenes, A. (2009). Scanning Flow CCN Analysis - A Method for Fast Measurements of CCN Spectra. Aerosol Sci. Tech. 43:1192-1207.

Moore, R. H., Nenes, A., Medina, J. (2010). Scanning Mobility CCN Analysis - A method for fast measurements of size resolved CCN distributions and activation kinetics. Aerosol Sci. Tech. 44:861-871.

Myrdal, P. B., Yalkowsky, S. H. (1997). Estimating pure component vapor pressures of complex organic molecules. Ind. Eng. Chem. Res. 36:2494-2499.

Nenes, A., Chuang, P.Y., Flagan, R.C., Seinfeld, J.H. (2001). A theoretical analysis of cloud condensation nucleus (CCN) instruments. J. Geophys. Res. 106:3449–3474.

Novakov, T., Penner, J. E. (2003). Large Contributions of Organic Aerosols to Cloud-Condensation Nuclei Concentrations. Nature. 365:823–826.

Orsini, D. A., Wiedensohler, A., Stratmann, F. (1998). A New Volatility Tandem Differential Mobility Analyzer to Measure the Volatile Sulfuric Acid Aerosol Fraction. J. Atmos. Ocean. Tech. 16:760-772.

Padró, L. T., Asa-Awuku, A., Morrison, R., Nenes, A. (2007). Inferring Thermodynamic Properties from CCN Activation Experiments: Single-component and Binary Aerosols. Atmos. Chem. Phys. 7:263–5274.

Patankar, S. V. (1980). Numerical heat transfer and fluid flow, New York, NY: McGraw-Hill.

Petters, M. D., Kreidenweis, S. M. (2007). A Single Parameter Representation of Hygroscopic Growth and Cloud Condensation Nucleus Activity. Atmos. Chem. Phys. 7:1961-1971.

Pope, F. D., Tong, H., Dennis-Smither, B. J., Griffiths, P. T., Clegg, S. L., Reid, J. P., Cox, R. A. (2010). Studies of single aerosol particles containing malonic acid, glutaric acid, and their mixtures with sodium chloride. II. Liquid-state vapor pressures of the acids. J. Phys. Chem. A. 114:10156-10165.

Prenni, A. J., DeMott, P. J., Kreidenweis, S. M., Sherman, D. E. (2001). The effects of low molecular weight dicarboxylic acids on cloud formation. J. Phys. Chem. A, 105:11240–11248.

Pye, H. O. T., Seinfeld, J. H. (2010) A global perspective on aerosol from low-volatility organic compounds. Atmos. Chem. Phys. 10:4377-4401.

Rader, D. J., McMurry, P. H. (1986). Application of the tandem differential mobility analyzer to studies of droplet growth or evaporation. J. Aerosol Sci. 17:771-787. doi:10.1016/0021-8502(86)90031-5.

Ravindran, P., Davis, E. J., Ray, A. K. (1979). Diffusivities of low-volatility species in light gases. AIChE J. 25:966-975.

Raymond, T. M., Pandis, S. N. (2002). Cloud activation of single-component organic aerosol particles, J. Geophys. Res., 107: 4787, doi:10.1029/2002JD002159.

Raymond, T. M., Pandis, S. N. (2003). Formation of cloud droplets by multicomponent organic particles. J. Geophys. Res. 108:4469. doi:10.1029/2003JD003503.

Riipinen, I., Koponen, I. K., Frank, G. P., Hyvarinen, A.-P., Vanhanen, J., Lihavainen, H., Lehtinen, K. E. J., Bilde, M.., Kulmala, M.., (2007) Adipic and malonic acid aqueous solutions: surface tensions and saturation vapor pressures. J. Phys. Chem. 111:12995–13002.

Riipinen, I., Pierce, J. R., Donahue, N. M., Pandis, S. N. (2010). Equilibration time scales of organic aerosol inside thermodenuders: Evaporation kinetics versus thermodynamics. Atmos. Environ. 44:597-607.

Riipinen, I., Pierce, J. R., Yli-Juuti, T., Nieminen, T., Häkkinen, S., Ehn, M., Junninen, H., Lehtipalo, K., Petäjä, T., Slowik, J., Chang, R., Shantz, N. C., Abbatt, J., Leaitch, W. R., Kerminen, V.-M., Worsnop, D. R., Pandis, S. N., Donahue, N. M., Kulmala, M. (2011). Organic condensation: a vital link connecting aerosol formation to cloud condensation nuclei (CCN) concentrations. Atmos. Chem. Phys. 11:3865-3878. doi:10.5194/acp-11-3865-2011.

Rissman, T.A., Varutbangkul, V., Surratt, J.D., Topping, D.O., McFiggans, G., Flagan, R.C., Seinfeld, J.H. (2007). Cloud condensation nucleus (CCN) behavior of organic aerosol particles generated by atomization of water and methanol solutions, Atmos. Chem. Phys., 7:2949-2971, doi:10.5194/acp-7-2949-2007.

Roelofs, G. J. (2008). A GCM study of organic matter in marine aerosol and its potential contribution to cloud drop activation. Atmos. Chem. Phys. 8:709-719.

Saleh, R., Shijadeh, A. (2007). Hygroscopic growth and evaporatioin in an aerosol with boundary heat and mass transfer. Aerosol Sci. 38:1-16.

Saleh, R., Shihadeh, A., Khlystov, A. (2010). Effect of aerosol generation method on measured saturation pressure and enthalpy of vaporization of dicarboxylic acid aerosols. Aerosol Sci. Tech. 44:302–307.

Saleh, R., Walker J., Khlystov A. (2008), Determination of saturation pressure and enthalpy of vaporization of semi-volatile aerosols: The integrated volume method. J. Aerosol Sci. 39:876-887.

Saleh, R., Shihadeh A., Khlystov A. (2009), Determination of evaporation coefficients of semi-volatile organic aerosols using an integrated volume—tandem differential mobility analysis (IV-TDMA) method. J. Aerosol Sci. 40:1019-1029.

Saleh, R., Shihadeh, A., Khlystov, A. (2011). On transport phenomena and equilibration time scales in thermodenuder. Atmos. Meas. Tech. 4:571-581. doi:10.5194/amt-4-571-2011.

Salo, K., Jonsson, A. M., Andersson, P. U., Hallquist, M. (2010), Aerosol Volatility and Enthalpy of Sublimation of Carboxylic Acids. J. Phys. Chem. A. 114:4586−4594.

Salo, K., Hallquist, M., Jonsson, Å. M., Saathoff, H., Naumann, K.-H., Spindler, C., Tillmann, R., Fuchs, H., Bohn, B., Rubach, F., Mentel, Th. F., Müller, L., Reinnig, M., Hoffmann, T., Donahue, N. M. (2011). Volatility of secondary organic aerosol during OH radical induced ageing. Atmos. Chem. Phys. 11:11055-11067.

Schwier, A. N., Sareen, N., Lathem, T., Nenes, A., McNeill, V. F. (2011). Ozone oxidation of oleate films decreases aerosol CCN activity. J. Geophys. Res. 116:D16202. doi:10.1029/2010JD015520.

Seinfeld, J. H., Pandis, S. (2006). Atmospheric Chemistry and Physics: from air pollution to climate change, Hoboken, N.J.: J. Wiley, 2nd ed.

Soonsin, V., Zardini, A. A., Marcolli, C., Zuend, A., Krieger, U. K. (2010). The vapor pressures and activities of dicarboxylic acids reconsidered: the impact of the physical state of the aerosol. Atmos. Chem. Phys. 10:11753-11767. doi:10.5194/acp-10-11753-2010.

Tao, Y., McMurry, P. (1989). Vapor pressures and surface free energies of C14-C18 monocarboxylic acids and C5 and C6 dicarboxylic acids. Environ. Sci. Tech. 23:1519.

Villani, P., Picard, D., Marchand N., Laj, P. (2007). Design and Validation of a 6-Volatility Tandem Differential Mobility Analyzer (VTDMA), Aerosol Sci. Tech., 41:898-906, doi: 10.1080/02786820701534593.

Virtanen, A., Joutsensaari, J., Koop, T., Kannosto, J., Yli-Pirila, P., Leskinen, J., Makela, J. M., Holopainen, J. K., Poeschl, U., Kulmala, M., Worsnop, D. R., Laaksonen, A. (2010). An amorphous solid state of biogenic secondary organic aerosol particles. Nature, 467:824 – 827, doi:10.1038/nature09455.

Wehner, B., Philippin, S., Wiedensohler, A. (2002). Design and calibration of a thermodenuder with an improved heating unit to measure the size-dependent volatile fraction of aerosol particles. J. Aerosol Sci. 33:1087-1093.

Yaws, C. L. (2003). Yaws' Handbook of thermodynamic and physical properties of chemical compounds. Knovel.

TABLES

Table 1. Thermodynamic and transport properties for investigated compounds

Organic Acid	Molar Mass (kg mol^{-1})	Density (kg m^{-3})	Diffusion Volume (cm^{-3})	Interfacial Energy (J m^{-2})*	Accommodation/Evaporation Coefficient**
Adipic Acid	0.14614	1362	140.72	0.06 (0.06)[A] 0.17 (0.12)[B] 0.032[C] 0.028[D]	0.10 (0.02)[B]
Azelaic Acid	0.18822	1251	202.1	0.18 (0.18)[A] 0.039[D]	-
Malonic Acid	0.10406	1616	79.34	0.02 (0.02)[A] 0.045[E]	-
Pimelic Acid	0.16017	1281	161.18	0.08 (0.08)[A] 0.23 (0.08)[B]	0.32 (0.05)[B]
Suberic Acid	0.17419	1272	181.64	0.1 (0.1)[A]	-
Succinic Acid	0.11809	1566	99.8	0.125 (0.125)[A] 0.15 (0.07)[B] 0.075[D] 0.045[E]	0.09 (0.02)[B]

*Absolute uncertainty in values is provided in brackets where available. Values obtained from temperature-dependent expressions at 50°C.

**α = 1 used in base model calculations

[A]Bilde et al. (2003)

[B]Saleh et al. (2009), adjusted up by 30% per Saleh et al. (2012)

[C]Riipinen et al. (2007), from temperature-dependent equation

[D]Yaws (2003), from temperature-dependent equation

[E]Hyvärinen et al. (2006), from temperature-dependent equation

Table 2. Reference saturation vapor pressure (at 298 K) and ΔH. C^* is calculated using properties from Table 1. Results of different model runs are identified by the surface tension (σ) source value and are also numbered consistently with Figure 7.

Organic Acid	σ (N m^{-1})	P^o(298K) (Pa×10^{-5})			ΔH (J mol^{-1}×10^{5})			C^*(298K) (µg m^{-3})	Uncert. (%)
		Max.	Min.	Avg.	Max.	Min.	Avg.		
Adipic Acid									
1: Bilde et al. (2003)	0.06	1.13	0.34	0.73	1.42	0.99	1.20	0.43	54
2: Riipinen et al. (2007)	0.032	1.21	0.36	0.78	1.41	0.99	1.20	0.46	54
3: Saleh et al. (2009)	0.17	0.82	0.23	0.52	1.47	1.01	1.24	0.31	57
4: Saleh et al. (2009)*	0.17	7.47	2.15	4.81	1.46	0.98	1.22	2.8	55
5: Yaws (2003)	0.028	1.20	0.35	0.78	1.41	0.99	1.20	0.46	55
Azelaic Acid									
6: Bilde et al. (2003)	0.18	0.63	0.26	0.44	1.47	1.14	1.31	0.34	41
7: Yaws (2003)	0.039	1.12	0.51	0.81	1.39	1.09	1.24	0.62	38
Malonic Acid									
8: Bilde et al. (2003)	0.02	10.13	6.57	8.35	1.38	1.16	1.27	3.5	21
9: Hyvärinen et al. (2006)	0.045	9.03	5.86	7.45	1.42	1.19	1.31	3.1	21
Suberic Acid									
10: Bilde et al. (2003)	0.1	0.19	-0.09	0.05	2.12	0.77	1.44	0.036	271
Succinic Acid									
11: Bilde et al. (2003)	0.125	5.90	1.97	3.93	1.21	0.74	0.98	1.9	50
12: Hyvärinen et al. (2006)	0.045	7.29	2.64	4.97	1.15	0.71	0.93	2.4	47
13: Saleh et al. (2009)	0.15	6.42	2.20	4.31	1.15	0.70	0.93	2.1	49
14: Saleh et al. (2009)*	0.15	68.40	25.20	46.80	1.12	0.68	0.90	22	46
15: Yaws (2003)	0.075	7.13	2.42	4.77	1.17	0.70	0.93	2.3	49

*Accommodation/evaporation coefficient changed from unity to available literature value

Table 3. Hygroscopicity values of pure organic compounds from this and published studies. Values in parentheses represent standard deviations unless indicated otherwise.

Organic Acid	κ_{By}	κ_{TD}	κ_{Tot}
Adipic Acid			
This work	0.022 (0.002)	0.024 (0.002)	0.023 (±0.002)
Kuwata et al. (2012)			0.002 (±0.001)[a]
Rissman et al. (2007)			0.059 (+0.021; -0.014)[b]
Huff Hartz et al. (2006)			0.003 (+0.002; -0.001)[b]
Broekhuizen et al. (2004)			0.096 (n/a)[c]
Raymond and Pandis (2002)			0.020 (+0.018; -0.008)[b, d]
Prenni et al. (2001)			0.014 (n/a)[b]
Corrigan and Novakov (1999)			0.030 (n/a)[b,d]
Cruz and Pandis (1997)			0.099 (+0.048; -0.029)[b, d]
Azelaic Acid			
This work	0.061 (0.007)	0.057 (0.005)	0.060 (±0.006)
Kuwata et al. (2012)			0.03 (±0.01)[a]
Huff Hartz et al. (2006)			0.022 (+0.018; -0.009)[b]
Malonic Acid			
This work	0.281 (0.034)	0.259 (0.052)	0.277 (±0.037)
Kumar et al. (2003)			0.227 (±0.028)
Prenni et al. (2001)			0.237 (n/a)[b]
Pimelic Acid			
This work	0.213 (0.016)	0.189 (0.014)	0.210 (±0.017)
Kuwata et al. (2012)			0.15 (±0.01)[a]
Frosch et al. (2010)			0.15 (±0.04)
Huff Hartz et al. (2006)			0.140 (+0.109; -0.054)[b]
Suberic Acid			
This work	0.007 (0.000)	n/a	0.007 (0.000)
Kuwata et al. (2012)			0.001 (n/a)[a]
Succinic Acid			
This work	0.285 (0.029)	0.239 (0.030)	0.273 (±0.035)
Rissman et al. (2007)			0.480 (+0.174; -0.117)[b]
Huff Hartz et al. (2006)			0.140 (+0.109; -0.054)[b]
Hori et al. (2003)			0.231 (±0.065)[e]
Prenni et al. (2001)			0.310 (n/a)[b]
Corrigan and Novakov (1999)			0.225 (n/a)[b,d]
Glutamic Acid			
This work	0.349 (0.004)	0.336 (0.016)	0.340 (±0.013)
Huff Hartz et al. (2006)			0.185 (+0.135;-0.069)[b]
Raymond and Pandis (2003)			0.337 (+0.304; -0.137)[b, d]

[a]average and standard deviation calculated using supplementary raw data corrected with ρ_{eff} when available
[b]uncertainty evaluated from spread in critical d_p using T=298 K and σ_w=0.072 J m^{-2}
[c]calculated for the pure metastable adipic acid data point; Petters and Kreidenweis (2007)
[d]averaged of data reported at multiple supersaturations
[e]standard deviation calculated from spread in the data; Petters and Kreidenweis (2007)

Figure Captions

Figure 1. Cross-sectional schematic of the thermodenuder constructed and used for this study.

Figure 2. (a) Thermodenuder centerline temperature profiles at unique temperature set points (T_{set}) and a flow rate of 1 L min^{-1}. Offline thermal probe measurement precision is 0.5°C. **(b)** Particle transmission efficiency through the thermodenuder compared to previously published values. Measurements correspond to 1 L min^{-1} flow through the instrument. The solid black line represents theoretical losses from Brownian diffusion.

Figure 3. Experimental setup for combined volatility and hygroscopicity measurements.

Figure 4. Simulated thermodenuder geometry and fields for inlet monodisperse adipic acid aerosol with 1000 cm^{-3} concentration, 0.6 L min^{-1} flow rate and 60°C set point in the heating section. (a) Thermodenuder geometry with sample streamlines and gridding system. (b) Simulated sizes for a 66 nm inlet diameter aerosol as a function of distance from the centerline. (c) Simulated size for 155 nm inlet aerosol flowing at streamline A at 1, 10, and 100 times the nominal inlet concentration. (d) is similar to (c), but for streamline B. Contour plots of simulated organic vapor (e) saturation ratio, (f) concentration, and (g) formation rate, assuming the cooling section is an impermeable wall. (h), (i), and (j) are similar to (e), (f), (g), respectively, but assuming the cooling section is a perfect sink of organic vapor.

Figure 5. Example size distributions measured from the thermodenuder (solid lines) and bypass (dotted lines) at 40 (blue), 50 (green), and 60°C (red) for azelaic acid with initial size of approximately 85 nm. Note that particle loadings vary between experiments.

Figure 6. Thermodenuder model response overlaid with laboratory observations for each volatility measurement considered. Solid curves represent the model evaluated at one set of the optimized parameters from Table 2. The dashed curves are model evaluations made at the upper and lower bounds of the uncertainty ranges in the retrieved parameters. The points plotted indicate corresponding inlet and outlet mode diameter values. Starred points represented data that was fitted to the model. Open circles separate from the starred points are data affected by non-volatile cores (and were not considered in the fitting procedure). Each colored set of curves and points represents measurements made at a particular temperature (indicated by the legend). Dashed curves indicate the uncertainty range of the model response.

Figure 7. Volatility parameters and sensitivity tests for select compounds compared against literature data. Blue bars/points indicate values obtained from measurements with each one corresponding to different rows of Table 2 corresponding to the indicated number. Red (magenta) bars refer to literature values reported for solid (liquid) phase data. Note that (b) excludes the outlier value from Cappa et al. (2007). Plotted literature data (letters) correspond to sources as follows: A (Bilde et al., 2003), B (Booth et al.,

2009), C (Booth et al., 2010), D (Booth et al., 2011), E (Cappa et al., 2007), F (Chattopadhyay et al., 2001), G (Pope et al., 2010), H (Riipinen et al., 2007), I (Saleh et al., 2009), J (Saleh et al., 2010), K (Salo et al., 2010), L (Soonsin et al., 2010).

FIGURES

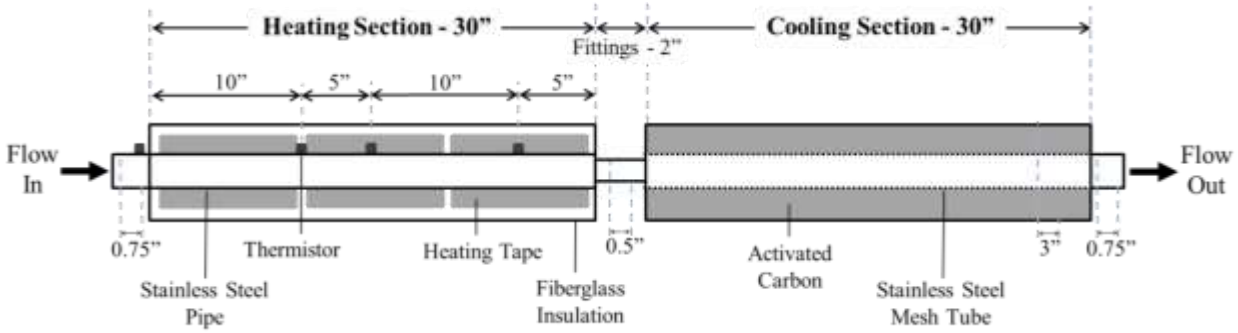

Figure 1

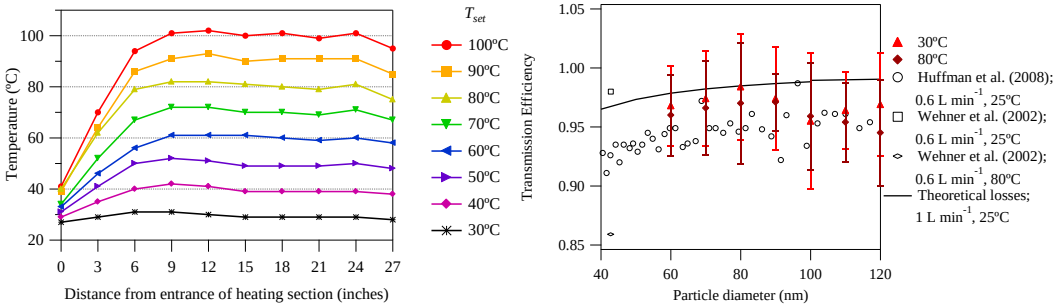
Temperature (ºC)
Distance from entrance of heating section (inches)
T_{set}
100ºC
90ºC
80ºC
70ºC
60ºC
50ºC
40ºC
30ºC
Transmission Efficiency
Particle diameter (nm)
30ºC
80ºC
Huffman et al. (2008); 0.6 L min-1, 25ºC
Wehner et al. (2002); 0.6 L min-1, 25ºC
Wehner et al. (2002); 0.6 L min-1, 80ºC
Theoretical losses; 1 L min-1, 25ºC

(a) (b)

Figure 2

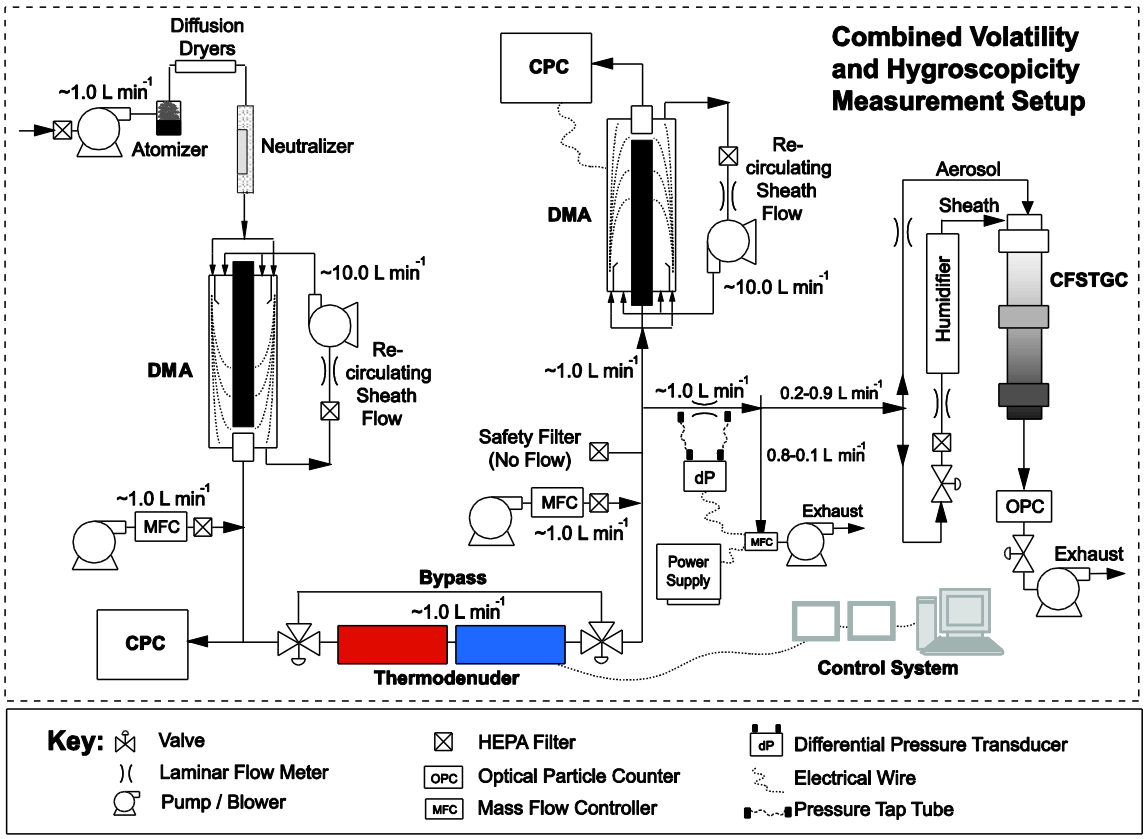
Combined Volatility and Hygroscopicity Measurement Setup
Diffusion Dryers
~1.0 L min-1
Atomizer
Neutralizer
DMA
~10.0 L min-1
Re-circulating Sheath Flow
~1.0 L min-1
MFC
CPC
Bypass
~1.0 L min-1
Thermodenuder
CPC
DMA
Re-circulating Sheath Flow
~10.0 L min-1
~1.0 L min-1
Safety Filter (No Flow)
MFC
~1.0 L min-1
~1.0 L min-1
0.2-0.9 L min-1
dP
0.8-0.1 L min-1
Exhaust
MFC
Power Supply
Aerosol
Sheath
Humidifier
CFSTGC
OPC
Exhaust
Control System
Key:
Valve
Laminar Flow Meter
Pump / Blower
HEPA Filter
OPC Optical Particle Counter
MFC Mass Flow Controller
dP Differential Pressure Transducer
Electrical Wire
Pressure Tap Tube

Figure 3

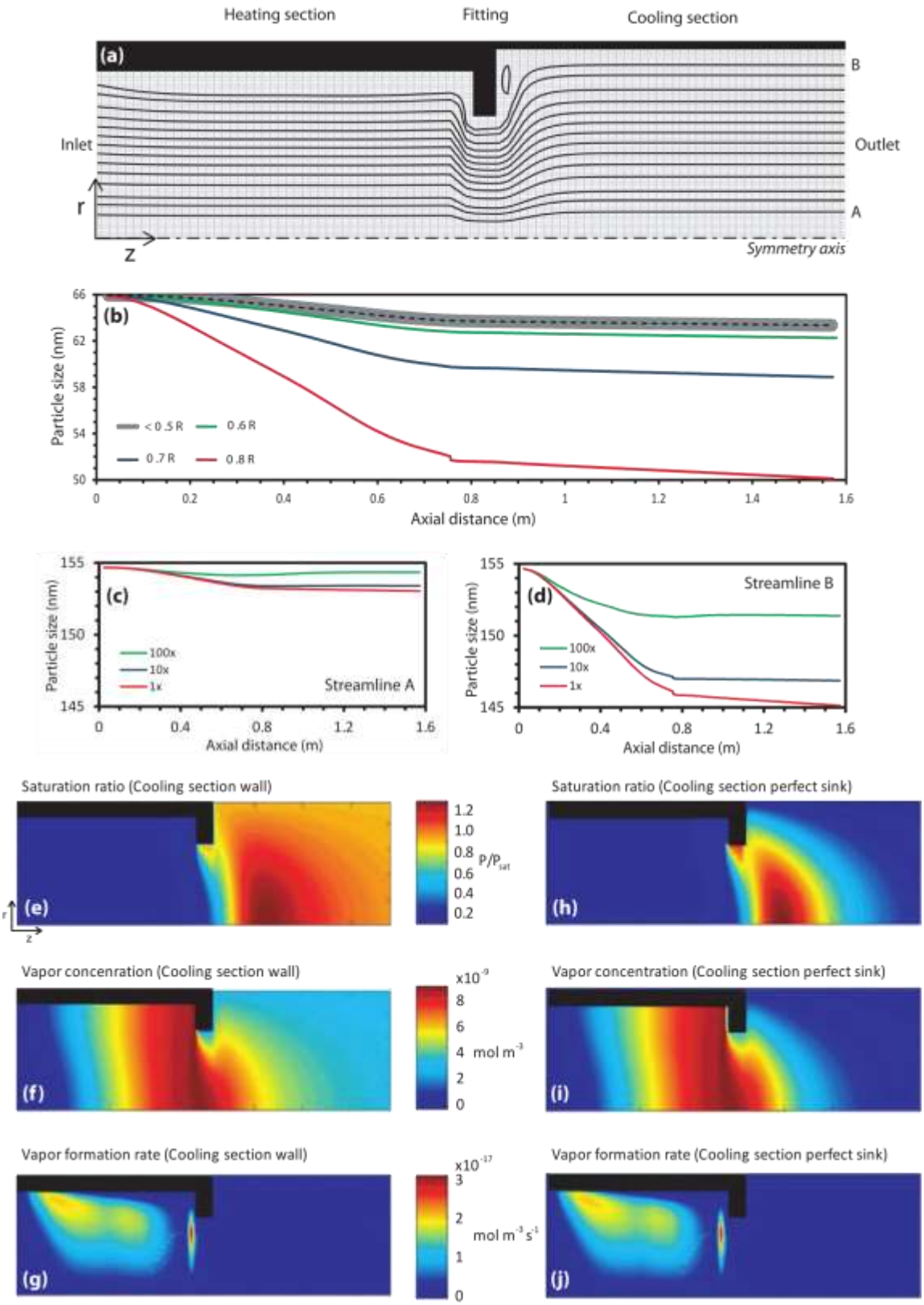
Heating section
Fitting
Cooling section
(a)
B
Inlet
Outlet
r
z
A
Symmetry axis
(b)
Particle size (nm)
< 0.5 R
0.6 R
0.7 R
0.8 R
Axial distance (m)
(c)
Streamline A
100x
10x
1x
(d)
Streamline B
Saturation ratio (Cooling section wall)
Saturation ratio (Cooling section perfect sink)
P/P_sat
(e)
(h)
Vapor concenration (Cooling section wall)
Vapor concentration (Cooling section perfect sink)
mol m^-3
(f)
(i)
Vapor formation rate (Cooling section wall)
Vapor formation rate (Cooling section perfect sink)
mol m^-3 s^-1
(g)
(j)

Figure 4

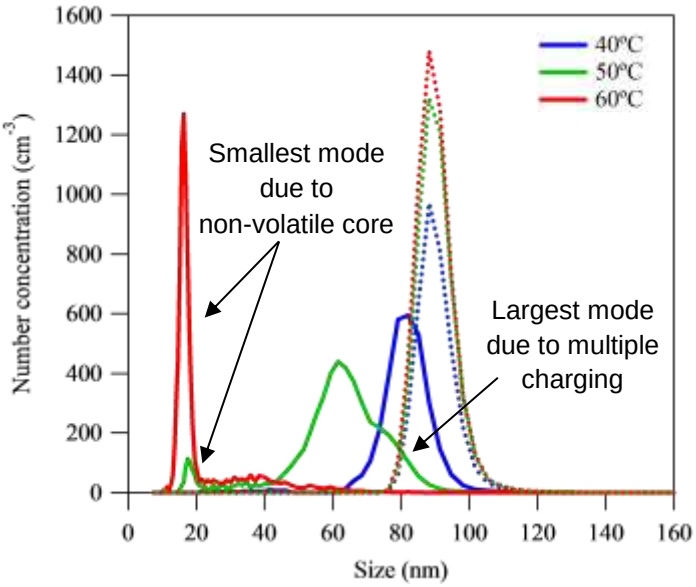
40°C
50°C
60°C
Smallest mode due to non-volatile core
Largest mode due to multiple charging
Number concentration (cm-3)
Size (nm)
0
200
400
600
800
1000
1200
1400
1600
0
20
40
60
80
100
120
140
160

Figure 5

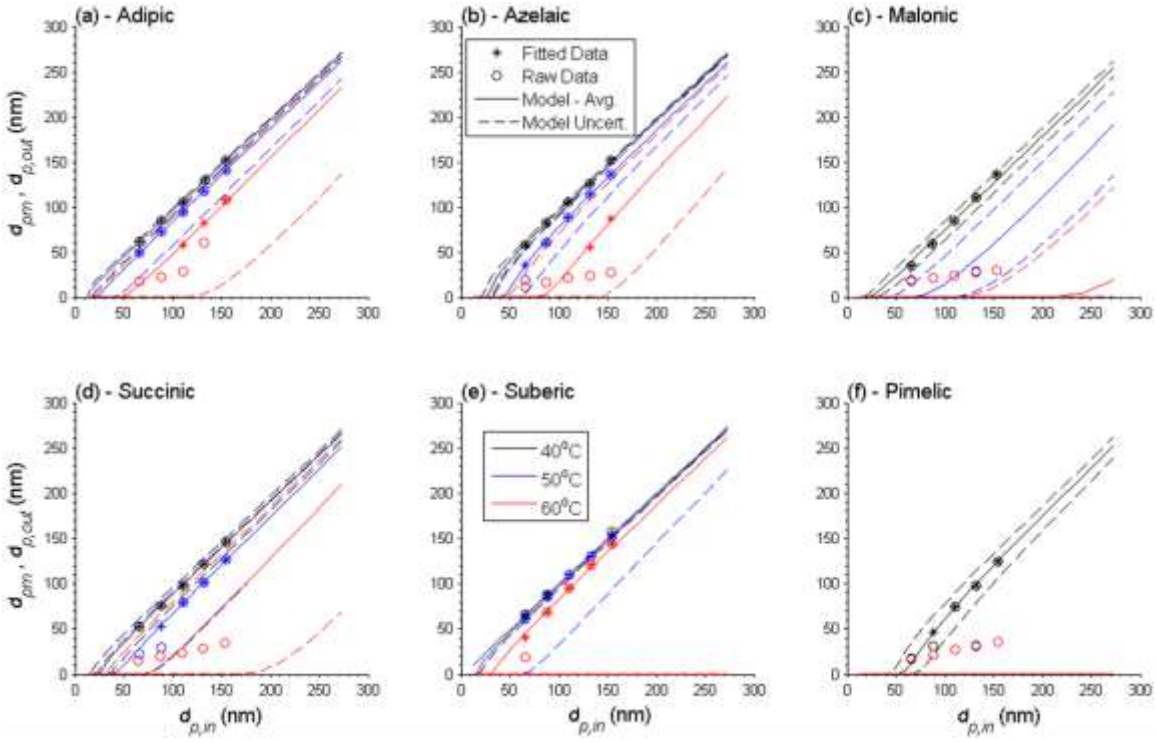
(a) - Adipic
(b) - Azelaic
(c) - Malonic
(d) - Succinic
(e) - Suberic
(f) - Pimelic
Fitted Data
Raw Data
Model - Avg
Model Uncert.
40°C
50°C
60°C
$d_{p,m}$, $d_{p,out}$ (nm)
$d_{p,in}$ (nm)

Figure 6

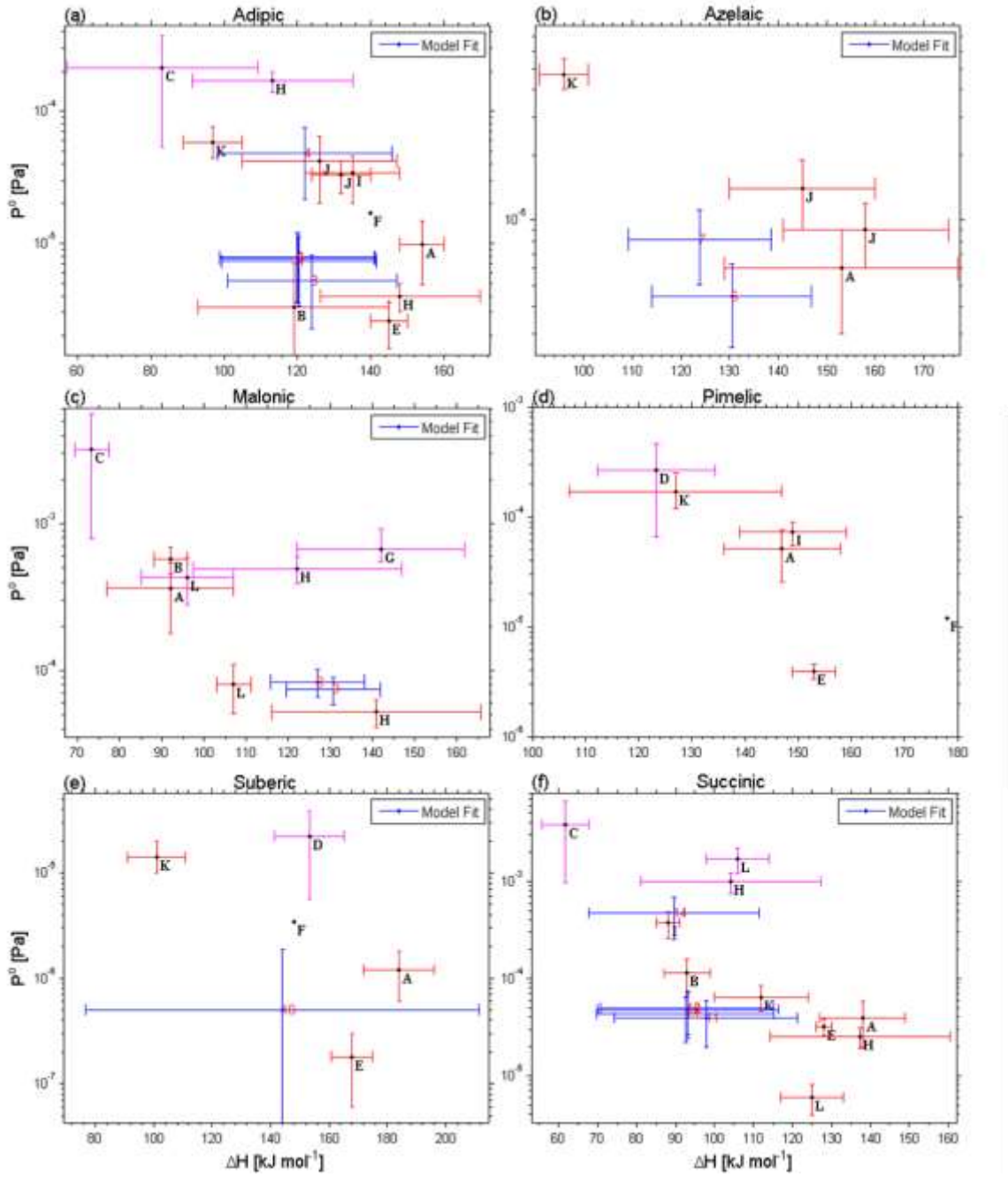
(a) Adipic
(b) Azelaic
(c) Malonic
(d) Pimelic
(e) Suberic
(f) Succinic
Model Fit
P⁰ [Pa]
ΔH [kJ mol⁻¹]

Figure 7